Research in Astronomy and Astrophysics, 22:015008 (11pp), 2022 January https://doi.org/10.1088/1674-4527/ac3325

Machine Learning for Improving Stellar Image-based Alignment in Wide-field Telescopes

Zhixu Wu[1], Yiming Zhang[1], Rongxin Tang[1], Zhengyang Li[2], Xiangyan Yuan[2], Yong Xia[1], Hua Bai[2], Bo Li[2], Zhou Chen[1], Xiangqun Cui[2], and Xiaohua Deng[1]

[1] Institute of Space Science and Technology, Nanchang University, Nanchang 330031, China

[2] Nanjing Institute of Astronomical Optics and Technology, Chinese Academy of Sciences, Nanjing 210042, China; zyli@niaot.ac.cn, xyyuan@niaot.ac.cn

Received 2021 August 5; revised 2021 October 12; accepted 2021 October 25; published 2022 January 21

Abstract

Stellar images will deteriorate dramatically when the sensitive elements of wide-field survey telescopes are misaligned during an observation, and active alignment is the key technology to maintain the high resolution of wide-field sky survey telescopes. Instead of traditional active alignment based on field-dependent wave front errors, this work proposes a machine learning alignment metrology based on stellar images of the scientific camera, which is more convenient and higher speed. We first theoretically confirm that the pattern of the point-spread function over the field is closely related to the misalignment status, and then the relationships are learned by two-step neural networks. After two-step active alignment, the position errors of misalignment parameters are less than 5 μm for decenter and less than 5″ for tip-tilt in more than 90% of the cases. The precise alignment results indicate that this metrology provides a low-cost and high-speed solution to maintain the image quality of wide-field sky survey telescopes during observation, thus implying important significance and broad application prospects.

Key words: telescopes – techniques: high angular resolution – techniques: miscellaneous

1. Introduction

In modern astronomy, such as time domain astronomy, and studies of black holes and dark energy (Copeland et al. 2006; Kasliwal et al. 2019; Yu 2020), high resolution is presumed for a sky survey telescope to accelerate discoveries in astronomy and astrophysics. As the field and aperture of sky survey telescopes increase, a primary mirror with a fast focal ratio is preferred to reduce the obscuration of the secondary mirror and decrease the length of the barrel, such as the J-PAS having a primary focal ratio of 1.5 (Benitez et al. 2014), the primary focal ratio of LSST is 1.18 (Sebag et al. 2016) and Mephisto is 1.3 (Li et al. 2020; Yuan et al. 2020). However, along with the fast focal ratio of the primary mirror, the secondary mirror will be more sensitive to misalignment and structural deformation caused by gravity and the temperature should be smaller.

The field-dependent aberration behaviors of a misaligned telescope with two or three mirrors were demonstrated by many works. Baranne and Wetherell et al. derived the formula of coma aberration for a non-coaxial dual-mirror system in 1972 (Crawford 1966; Wetherell & Rimmer 1972). For the more common situation, Dingqiang Su analyzed the coma aberration of a non-coaxial dual-mirror system when the secondary mirror with decent and tip-tilt and the two axials of the secondary mirror and primary mirror do not lie in the same plane, and proved that the coma aberrations can be operated on like vectors (Su 1989). According to Nodal Aberration Theory, which was first reported by Shack and Thompson (Shack & Thompson 1980; Thompson et al. 2008), orthogonal Zernike polynomials were widely used for the numerical expression of field-dependent aberrations. Algorithms such as reverse-optimization, damped least-squares (Lee et al. 2007; Bloemhof et al. 2012; Li et al. 2015a, 2015b) and principal component analysis can deliver suitable corrections for resolving misalignments with relatively high accuracy.

Unfortunately, acquisitions of field aberrations are difficult during telescope observations and complex wave front sensing systems have to be equipped for measuring the field aberrations. Four edge field curvature wave front sensors at the focal plane are most commonly employed for wide-field imagers with high image quality, such as the Javalambre Survey Telescope (JST/T250) and Large Synoptic Survey Telescope (LSST) (Manuel et al. 2010; Chueca et al. 2012; Claver et al. 2012; Xin et al. 2015). However, it is easy for a beam splitting system, which is required for the traditional curvature wave front sensor, to measure the in-focus and out-of-focus images, to produce vignetting due to the fast focal ratio. The split curvature wave front sensors need to compensate for the inherent aberrations of the two sources with different fields of view (FOVs) and require expensive CCD stitching technology, which significantly increases the cost of the camera.

Instead of detecting the field wave front errors, the pattern of the point-spread function (PSF) ellipticity distribution also reveals the system's misaligned status (Bo 2021, Zhang 2016)

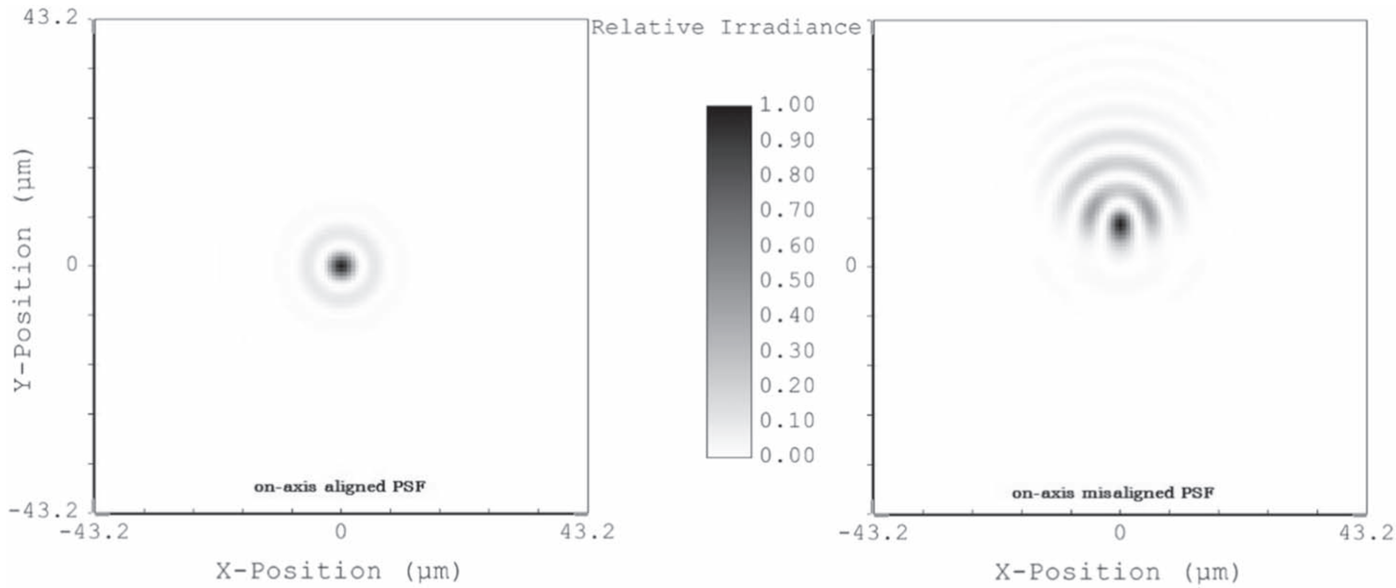

Figure 1. PSF representation in the image plane for the situation with or without misalignment. The PSF image on the left shows a standard airy disk formed by an ideal optical system; the right image is a PSF of an optical system with coma aberration.

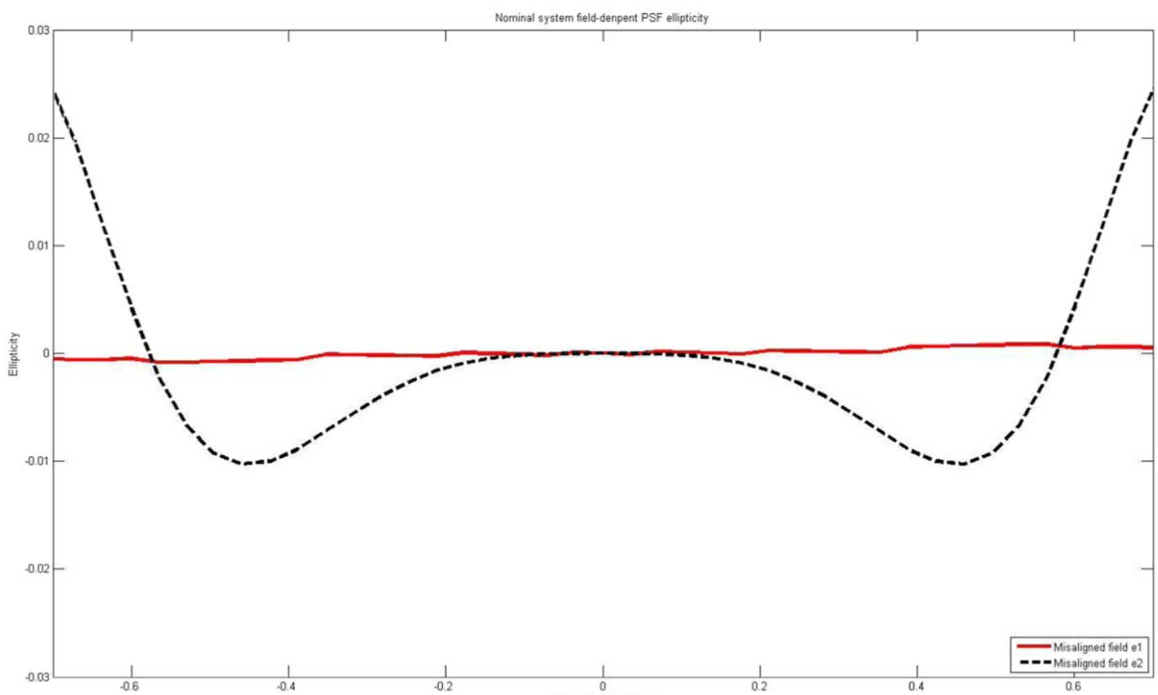

Figure 2. PSF ellipticity e1 and e2 over the diagonal FOV of the nominal design. The range of the diagonal FOV is from $(-0.^\circ7, -0.^\circ7)$ to $(0.^\circ7, 0.^\circ7)$. The distribution patterns of e1 and e2 are symmetrical.

and measuring the PSF of the scientific images seems to be more convenient (Luppino & Kaiser 1997). In this work, machine learning alignment metrology is proposed for calculating the misalignment parameters based on the stellar images of wide-field telescopes, and we employ a relatively complex Ritchey–Chrétien (R-C) configuration (Mephisto) to model the alignment metrology. The optical system is perturbed with various sets of misalignments, delivering a misaligned field-dependent PSF, and the explicit mathematical model between misalignments and the pattern of field-dependent PSF is complex and hard to establish. Machine learning is a method of data analysis that automates analytical

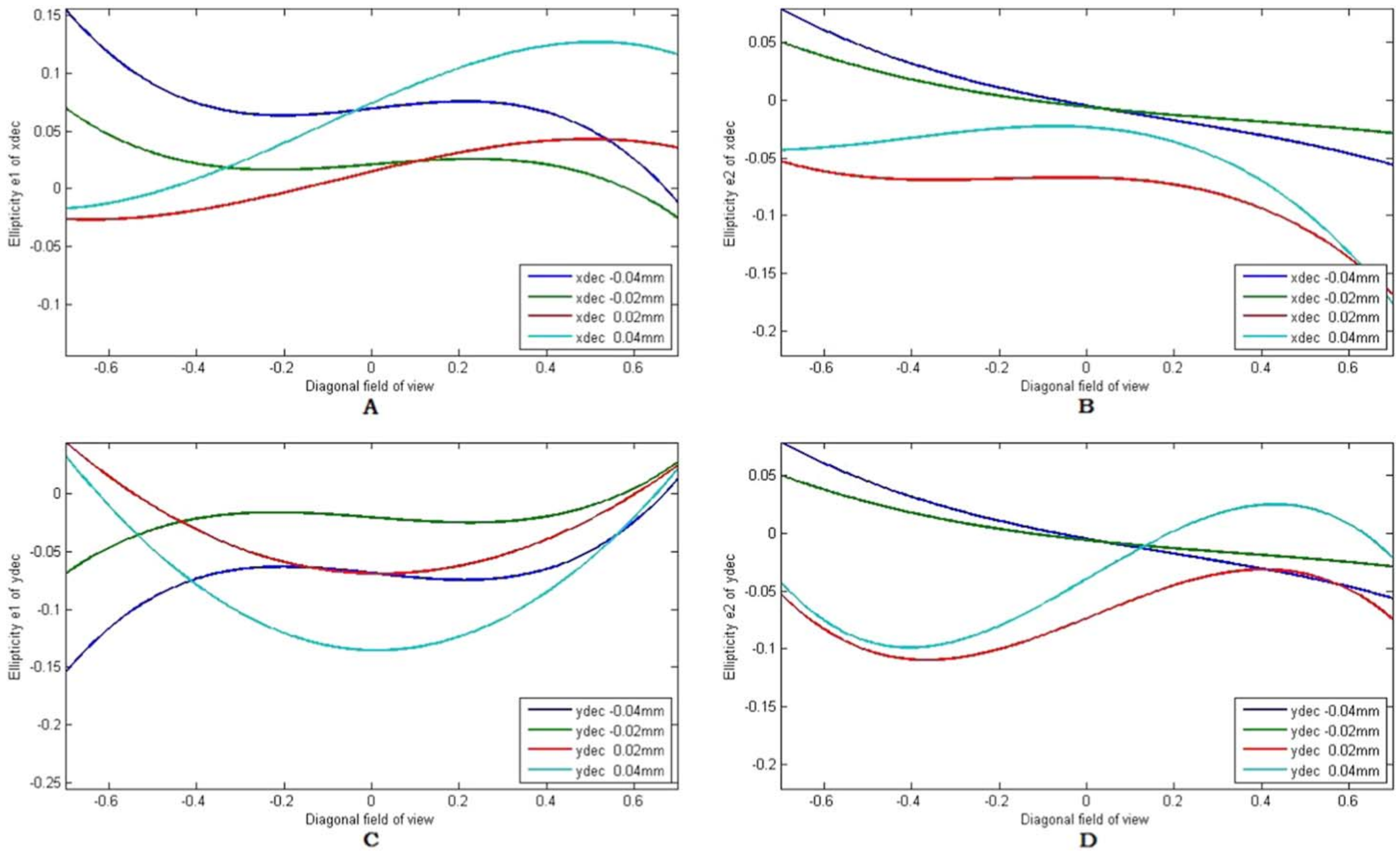

Figure 3. PSF ellipticity e1 and e2 with decentering (X, Y) of the secondary mirror. The range of the diagonal FOV is from $(-0.^{\circ}7, -0.^{\circ}7)$ to $(0.^{\circ}7, 0.^{\circ}7)$. (A), (B) The distribution patterns of e1 and e2 when the secondary mirror of the optical system has x-decent misalignment. (C), (D) The e1 and e2 patterns of the secondary mirror with y-decent. It is confirmed that the symmetric features no longer exist due to the decent misalignment of the secondary mirror.

model building (Chen et al. 2019; Tang et al. 2020), and the nonlinear nature of neural networks along with their inherent flexibility and adaptability makes them good candidates for stellar image-based alignment that are not easily solved with conventional algorithms. Compared with the traditional active alignment metrology based on field-dependent aberrations, there are some advantages. First, the active alignment system can be simplified because the wave front sensor system has been removed. Second, because of the one-to-one correspondence between the stellar images of the CCD and the output misalignment parameters, the calculation time spent on the wave front reconstruction and misalignment parameter calculation that form field dependent wave front error can be avoided, which improves the response speed of the active alignment.

2. Method

2.1. The Pattern Variations of the PSF Resulting from Misalignment

Generally, a stellar image is a convolution of an ideal point source and the PSF. The wave front expression for the misaligned optical system is given by Equation (1) as:

$$
\begin{aligned}
W = \sum_{j}\sum_{p=0}^{\infty}\sum_{n=0}^{\infty}\sum_{m=0}^{\infty}(W_{klm})\\
\times [(\boldsymbol{H} - \sigma_{\boldsymbol{j}})\bullet(\boldsymbol{H} - \sigma_{\boldsymbol{j}})]^{p}\\
\times (\rho\bullet\rho)^{n}[(\boldsymbol{H} - \sigma_{\boldsymbol{j}})\bullet\rho]^{m}
\end{aligned} \quad (1)
$$

where W_{klm} is the aberration coefficient, $\boldsymbol{H}$ represents the normalized image field position, ρ is the normalized pupil position and $\sigma_{\boldsymbol{j}}$ denotes the aberration field center shifting vector of $\boldsymbol{j}$ elements, additionally, $k = 2p + m$, $l = 2n + m$. If i represents the total misaligned degrees of freedom of a misaligned system, for any field of the optical system, the wave front aberration at the pupil is obtained from Equation (2) as:

$$W = W(\delta_1, \delta_2,\ldots,\delta_i, \rho) \quad (2)$$

where $p(\rho)$ is the pupil function, and the generalized pupil function $P(\delta_1, \delta_2,\ldots,\delta_i, \rho)$ is therefore given by Equation (3)

$$
\begin{aligned}
&P(\delta_1, \delta_2,\ldots,\delta_i, \rho)\\
&= p(\rho)\exp jW(\delta_1, \delta_2,\ldots,\delta_i, \rho).
\end{aligned} \quad (3)
$$

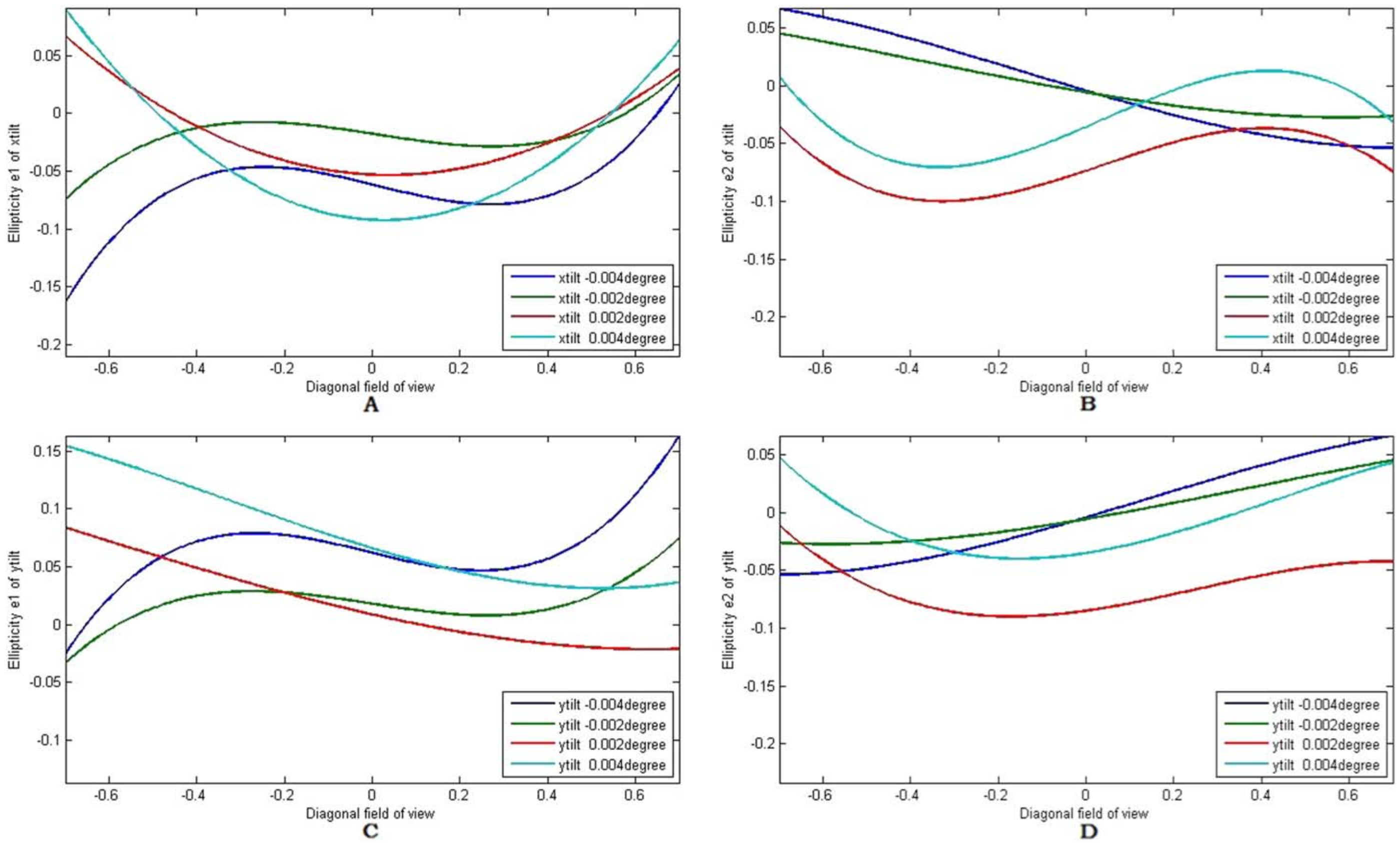

Figure 4. PSF ellipticity e1 and e2 with tilt (X, Y) of the secondary mirror. The range of the diagonal FOV is from ($-0^{\circ}.7$, $-0^{\circ}.7$) to ($0^{\circ}.7$, $0^{\circ}.7$). (A) and (B) display the distribution patterns of e1 and e2 when the secondary mirror of the optical system has x-tilt misalignment; (C) and (D) are the e1 and e2 patterns of the secondary mirror with y-tilt. The symmetric features have also disappeared.

Table 1
Specifications for Mephisto Including Optics, Aperture, Focal Ratio, the FOV, Pixel Scale and Image Quality

ITEM	Specifications
Optics	R-C with field corrector
Aperture	1.6 m (diameter)
Focal ratio	4.5
FOV	2° (diameter)
Pixel scale	$0.286''/10\ \mu$m
Image quality	80%EE $\leqslant 0.6''$

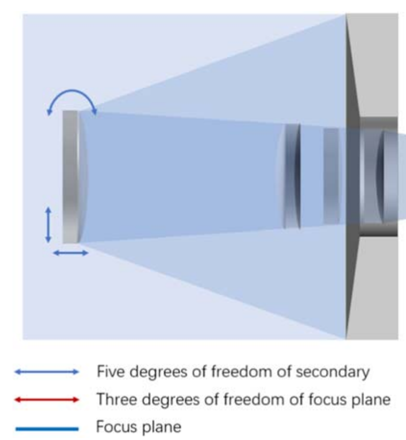

Figure 5. Layout of the misalignment perturbations of Mephisto. The 5 rigid body DOFs of M2 contain x-decent, y-decent, x-tilt, y-tilt and piston; the 3 rigid body DOFs of the camera are x-tilt, y-tilt and piston.

The amplitude spread function $h(\boldsymbol{H})$ is a Fourier transform of the generalized pupil function shown in Equation (4)

$$h(\boldsymbol{H}) = \mathrm{FFT}(P(\delta_1, \delta_2,\ldots,\delta_i, \rho)) \tag{4}$$

$$\mathrm{PSF}(\delta_1, \delta_2,\ldots,\delta_i, \boldsymbol{H}) = |h(\delta_1, \delta_2,\ldots,\delta_i, \boldsymbol{H})|^2. \tag{5}$$

The PSF distribution in the image plane, which is shown in Figure 1, is related to the misalignments (δ_1, δ_2,…,δ_i). To numerically investigate the PSF distribution, a measurable parameter termed ellipticity is adopted. This term was previously used in weak lensing research for describing the

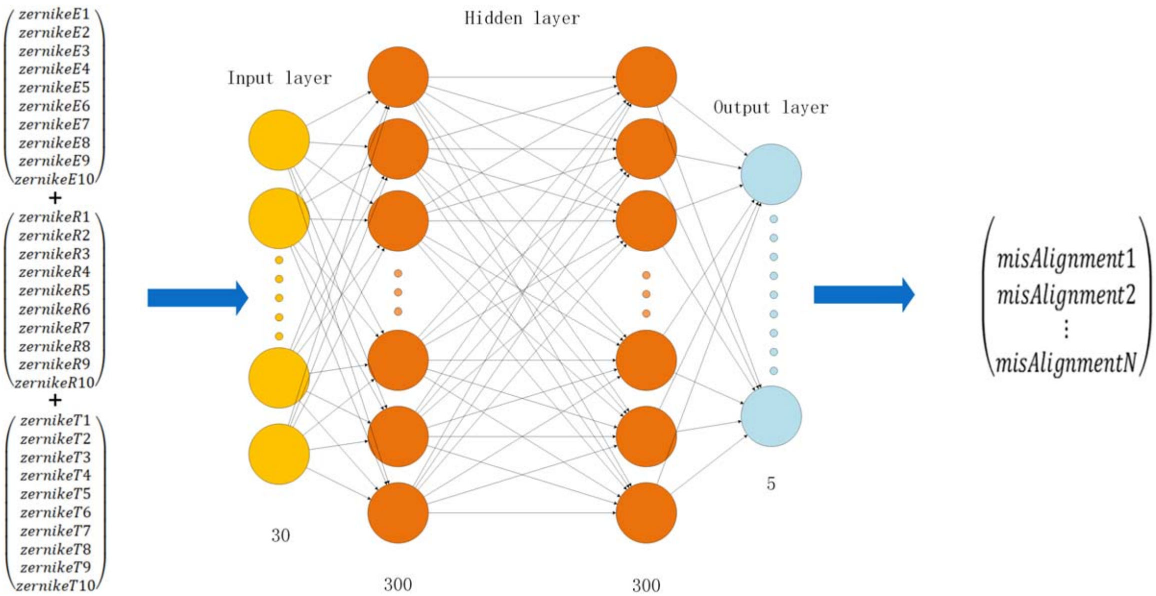

Figure 6. The network architecture of the coarse neural network and fine neural network. The architecture of the two networks is identical. The number of nodes for the input layer is 30; each hidden layer contains 300 nodes; the output layer contains 8 nodes.

shape of galaxies (Luppino & Kaiser 1997)

$$\begin{cases} Q_{i,j} = \iint_{(H_x,H_y)} \mathrm{weight}(H_x, H_y)\mathrm{PSF}(\delta_1, \delta_2,\ldots,\delta_i, H_x, H_y) H_x H_y dH_x dH_y \\ e_\alpha = \dfrac{Q_\alpha}{T}. \end{cases} \tag{6}$$

In Equation (6), $\alpha = 1\, or\, 2$, $H_1 = H_x - H_{\mathrm{xcenter}}$, $H_2 = H_y - H_{\mathrm{ycenter}}$, $Q_1 = Q_{11} - Q_{22}$, $T = Q_{11} + Q_{22}$. Hence, with PSF acquisition at an FOV (H_{x0}, H_{y0}), the numerical ellipticity is expressed as:

$$\begin{cases} E_{10} = e_1(\delta_1, \delta_2,\ldots,\delta_i, H_{x0}, H_{y0}) \\ E_{20} = e_2(\delta_1, \delta_2,\ldots,\delta_i, H_{x0}, H_{y0}). \end{cases} \tag{7}$$

In addition to ellipticity, full width at half maximum R and azimuth θ are also parameters that can numerically describe the PSF

$$\begin{cases} e = \dfrac{Q_{ii} - Q_{jj} + 2iQ_{ij}}{Q_{ii} + Q_{jj}} \\ R = \sqrt{Q_{ii} + Q_{jj}} \\ \theta = \tan^{-1}\dfrac{2Q_{ij}}{Q_{ii} - Q_{jj}}. \end{cases} \tag{8}$$

Figure 2 demonstrates that the distribution patterns of PSF ellipticity e1 and e2 over the diagonal FOV are symmetrical. To illustrate the field-dependent PSF variations resulting from misalignment, we deliberately perturbed the secondary mirror of Mephisto and recorded e1 and e2 at diagonal FOVs. Figures 3(A) and (B) demonstrate that e1 and e2 vary from an FOV of (–0°.7, –0°.7) to an FOV of (0°.7, 0°.7) with secondary mirror decenter values of −0.04, −0.02, 0.02 and 0.04 mm at the sagittal surface; Figures 3(C) and (D) affirm that e1 and e2 vary from an FOV of (–0°.7, –0°.7) to an FOV of (0°.7, 0°.7) with secondary mirror decenter values of –0.04, –0.02, 0.02 and 0.04 mm at the meridian surface. Figures 4(A)–(D) display PSF ellipticity e1 and e2 when the secondary mirror of the optical system has x-tilt and y-tilt misalignments.

The perturbation parameter curves reveal that: (1) misalignment destroys the symmetry of the ellipticity distribution; (2) over the FOV, the ellipticity variations are continuous; (3) the secondary decenter in the sagittal surface may couple in tilt in the meridian surface; (4) the ellipticity distributions vary nonlinearly with the misalignments. Based on the observations above, calculating the misalignments by mapping the PSF distribution of a scientific image is feasible.

2.2. Machine Learning for Active Alignment

2.2.1. Generation of the Training Dataset

Machine learning is essentially a data-driven method that requires a large amount of field-dependent PSF and corresponding misalignment parameters to feed the neural networks. Because different telescopes have different optical configurations, a deep learning model trained with one particular telescope cannot be adjusted and transferred to another telescope. To obtain the neural network model for one specific telescope, a customized training data set of Mephisto is

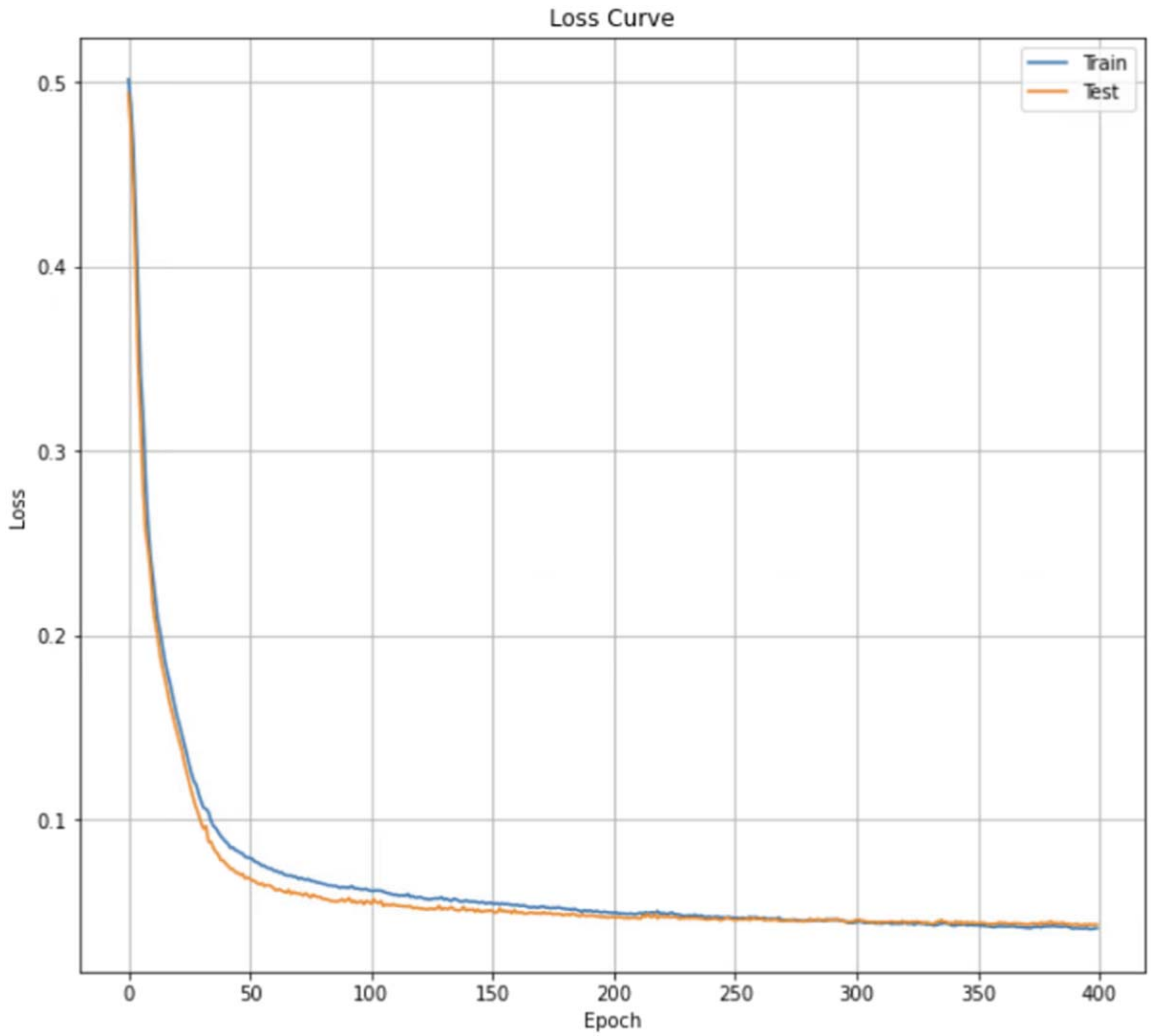

Figure 7. Loss function curve of the neural network. The loss function converged after 400 epochs of training.

necessary. Mephisto was developed for Yunnan University. It combines a large aperture with a wide FOV for rapid survey while ensuring an optical imaging quality suitable for precise photometry. The innovative optical design guarantees an ambitious project enabling the observations of three colors simultaneously, with wavelengths ranging from 320 nm to 1000 nm. The specifications of Mephisto are presented in Table 1, while the optical design of Mephisto and the misalignment perturbations of Mephisto are demonstrated in Figure 5.

In Mephisto, there are 8 degrees of freedom (DOFs) for perturbations, which include 5 rigid body DOFs of M2 and 3 rigid body DOFs of the camera. The hexapod microrobots are applied on the M2 and the camera to compensate for rigid body misalignments. The acquisition of training data is automatically executed by Dynamic Data Exchange (DDE) between MATLAB and ZEMAX. First, 8 DOFs for perturbations with different sensitivities are generated randomly through MATLAB. Second, these misaligned parameters are set into ZEMAX by DDE programming. Third, the focal plane is partitioned into m•m equal tiles, PSF in the center of each tile is generated by ray tracing in ZEMAX and imported into MATLAB, and this PSF is described in terms of measurable parameters. Assuming that the misalignment state of Mephisto is s_I, 3•m^2 measurable parameters of the PSF can be expressed as:

$$(e_{s_i f_1},\ e_{s_i f_2}, \cdots\cdots, e_{s_i f_m}, \cdots\cdots, e_{s_i f_{m^2}}) \tag{9}$$

$$(\theta_{s_i f_1},\ \theta_{s_i f_2}, \cdots\cdots, \theta_{s_i f_m}, \cdots\cdots, \theta_{s_i f_{m^2}}) \tag{10}$$

$$(r_{s_i f_1},\ r_{s_i f_2}, \cdots\cdots, r_{s_i f_m}, \cdots\cdots, r_{s_i f_{m^2}}). \tag{11}$$

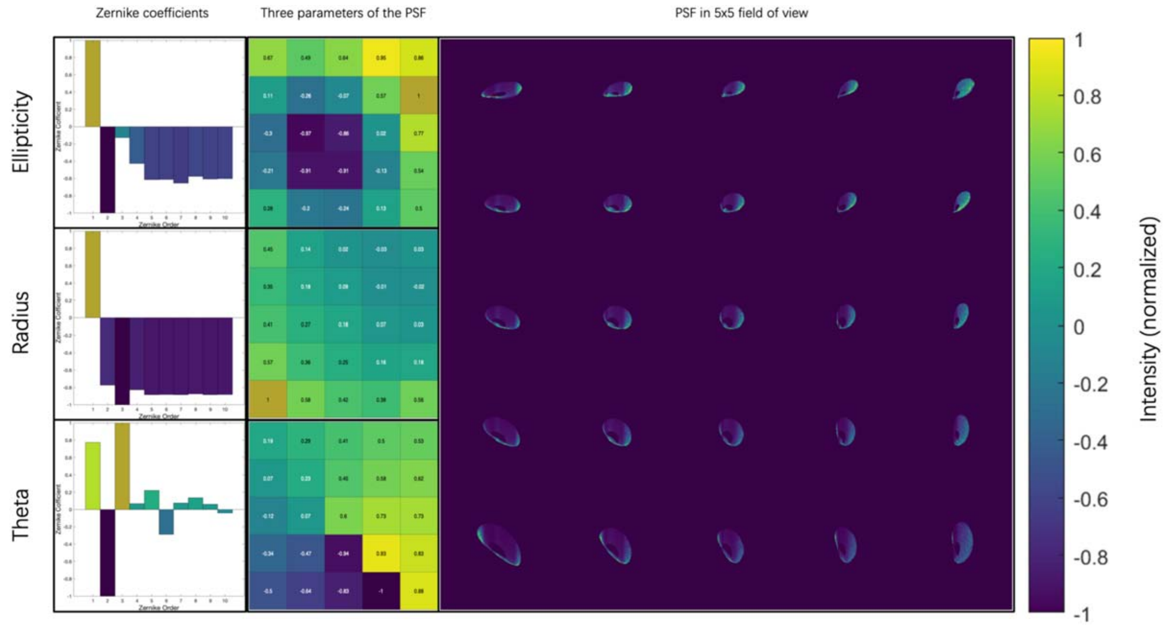

Figure 8. PSF, parameters of PSF and Zernike coefficients before correction. The right column is the PSF images of 25 FOVs; the middle column shows the calculated three parameters of the 25 PSFs, and the three parameters are ellipticity, radius and theta; the left column is the fitted Zernike coefficients of the three parameters in the middle column. It is noticeable that all parameters have no units due to the normalization.

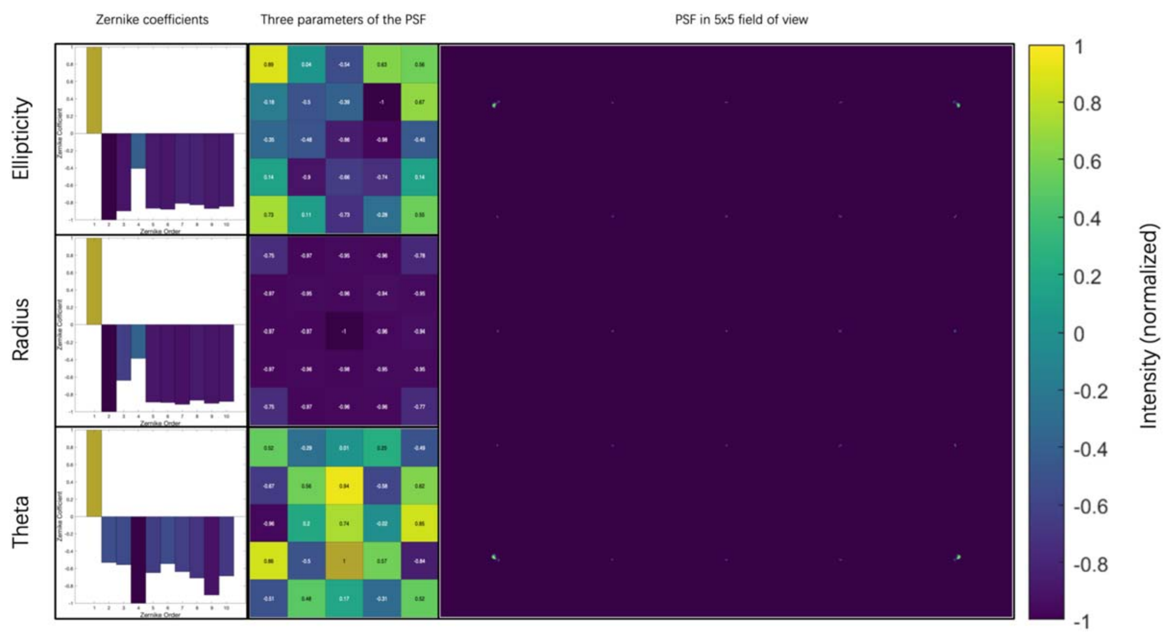

Figure 9. PSF, parameters of PSF and Zernike coefficients after correction. It is shown that the performance of the system has improved greatly after the stellar image-based alignment.

Because the stellar images are distributed randomly on the CCD, the random positions of the stellar images will significantly increase the learning complexity and scale of deep learning. In a coaxial optical system, the pattern of the field-dependent PSF is generally distributed axially symmetrically, which means that the pattern is distributed symmetrically around the center point, and the symmetrical pattern will be broken when the co-axial optical system is misaligned. This phenomenon is very similar to field-dependent aberrations. Analogous to the vector aberration

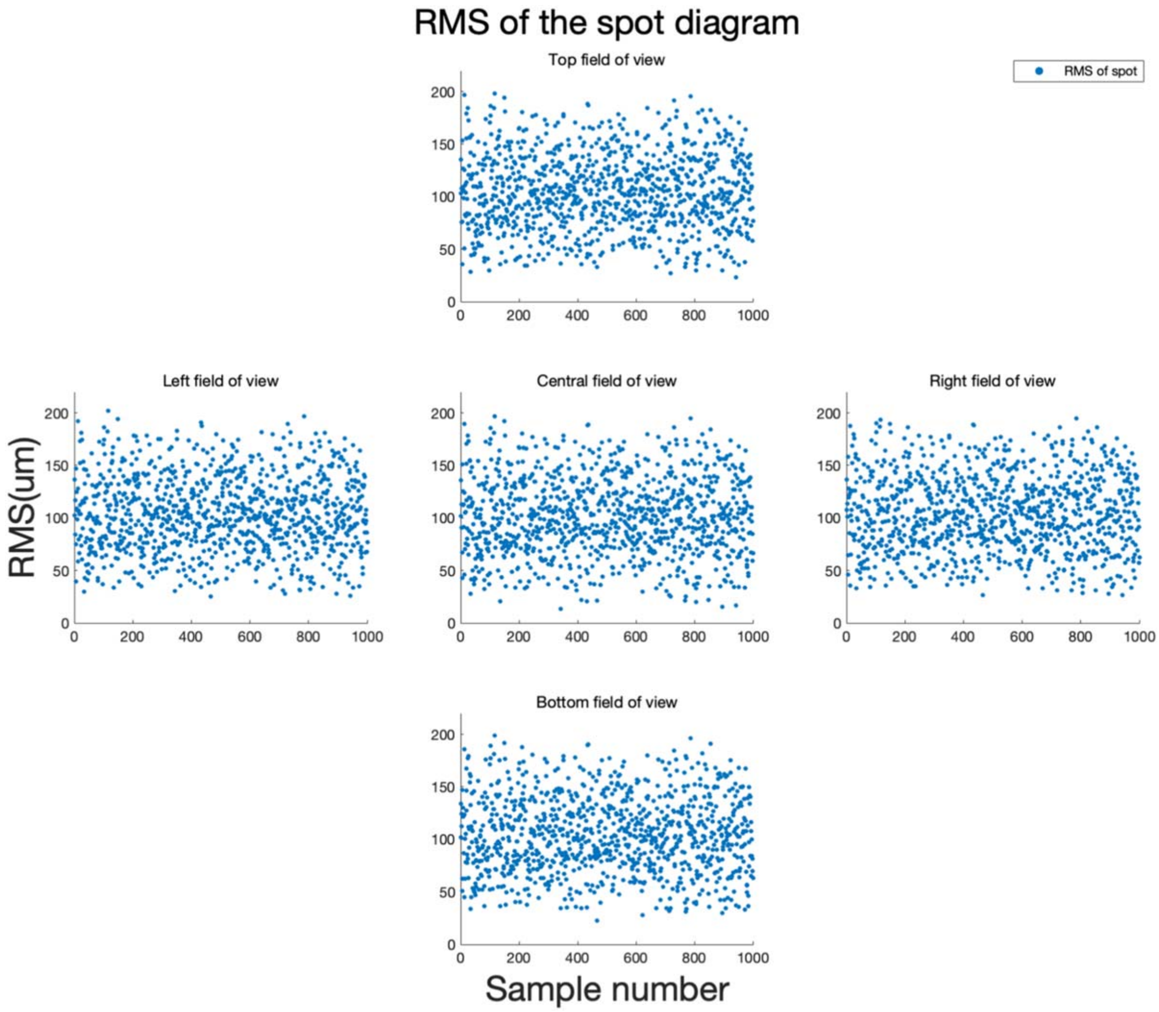

Figure 10. rms of the spot diagram before correction. The five subfigures describe the distribution of the PSF's rms of 1000 testing samples at five FOVs. These five FOVs contain four corner FOVs of (1°, 0°), (0°, 1°), (−1°, 0°), (0°, −1°), and one center FOV of (0°, 0°). The rms of the spot diagram is distributed randomly in the range of 50–200 μm.

theory, the $3\bullet m^2$ measurable parameters are also fitted by a low-order Zernike polynomial to 3 × parameters in this work.

2.2.2. Network Architecture

To improve the training efficiency, two-step calibration by coarse and fine neural networks is used in this work. The telescope is calibrated first by the coarse neural network, and then the hexapod microrobots compensate for the rigid body motions according to the parameters outputted by the fine neural network. The coarse network has an identical architecture as the fine network, but with different training ranges. The network architecture is depicted in Figure 6. Each hidden layer contains 300 nodes, the input layer has 30 input nodes for low-order Zernike polynomial coefficients, and the output layer contains 8 output nodes for the misalignment parameters.

Since the three measurable parameters of the PSF are in different ranges and the sensitivities of each misalignment parameter are different, normalization is necessary to ensure that all input vectors and the output misalignment parameters are within the same scale. It is noticeable that the original scale of the input training data is saved, thus the normalization will not affect the relationship between the pattern of the PSF over the field and the misalignment status. The normalization is expressed as:

$$X_{\mathrm{scaled}} = \frac{X - X_{\mathrm{mean}}}{X_{\mathrm{std}}} \tag{12}$$

where X_{scaled} is the normalized data set, X is the original data set, X_{mean} is the mean value of the original data set and X_{std} is the standard deviation of the original data set.

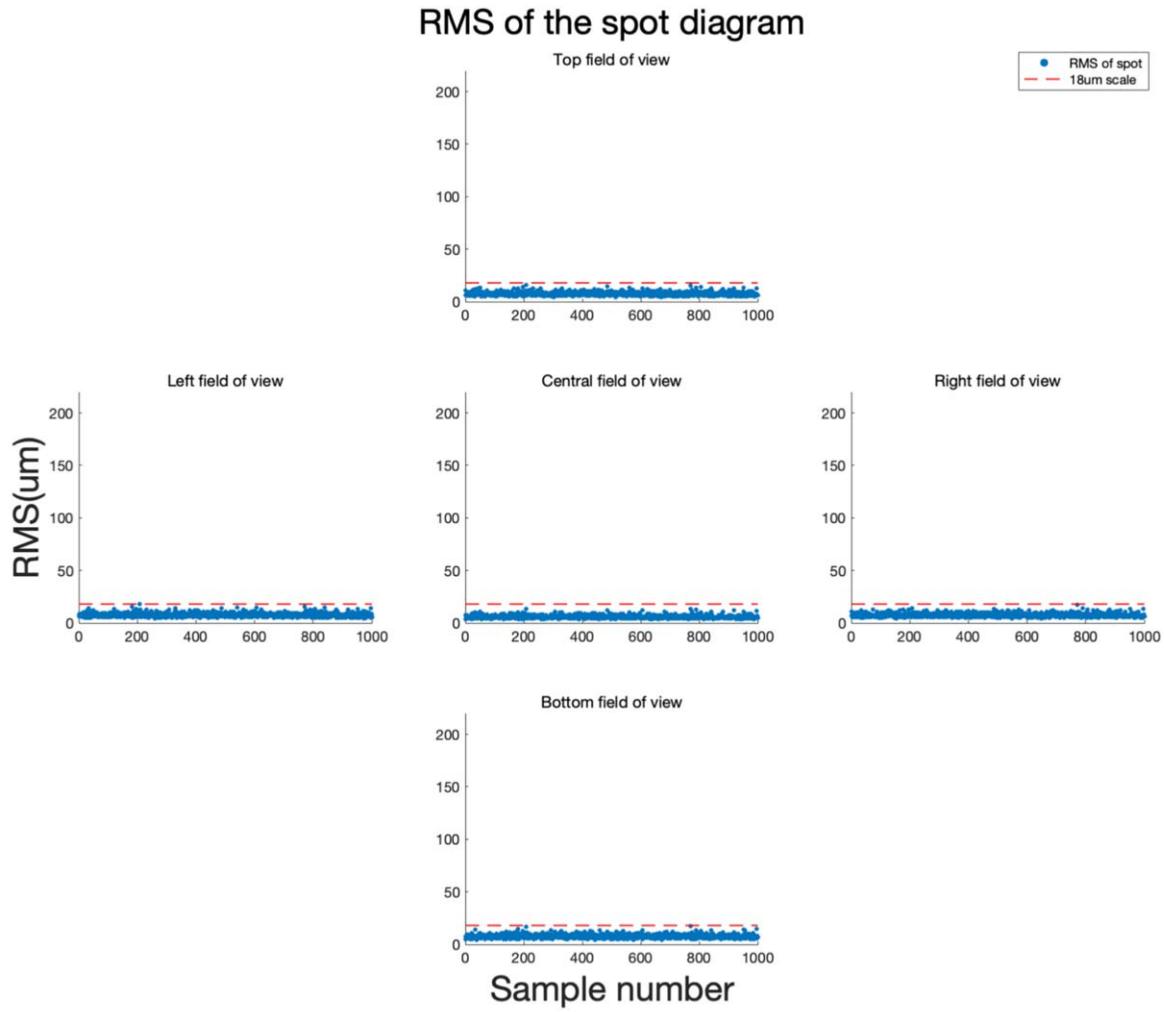

Figure 11. rms of the spot diagram after correction. The five subfigures describe the distribution of the PSF's rms of 1000 testing samples at five FOVs. These five FOVs contain four corner FOVs of (1°, 0°), (0°, 1°), (−1°, 0°), (0°, −1°), and one center FOV of (0°, 0°). After two-step active alignment, the rms is mainly below 18 μm.

Neural networks are trained using stochastic gradient descent of the loss function. Two kinds of loss functions, MAE loss function and Log-cosh loss function, are utilized in this work. The stochastic gradient descent of the loss function can be expressed as:

$$\begin{cases} w_{ij}^{L} = w_{ij}^{L} - \alpha \dfrac{\partial}{\partial w_{ij}^{L}} \mathrm{Loss}_{\mathrm{Fun}} \\ b_{i}^{L} = b_{i}^{L} - \alpha \dfrac{\partial}{\partial b_{i}^{L}} \mathrm{Loss}_{\mathrm{Fun}} \end{cases} \tag{13}$$

$$\mathrm{Loss}_{\mathrm{Fun}} = \begin{cases} \mathrm{MAE}(\mathrm{Net}_i^{\mathrm{In}}, \mathrm{Net}_i^{\mathrm{Out}}) = \dfrac{\sum_{i=1}^{n} |\mathrm{Net}_i^{\mathrm{In}} - \mathrm{Net}_i^{\mathrm{Out}}|}{n} \\ \mathrm{LogCosh}(\mathrm{Net}_i^{\mathrm{In}}, \mathrm{Net}_i^{\mathrm{Out}}) = \sum_{i=0}^{n} \log(\cosh \mathrm{Net}_i^{\mathrm{In}} - \mathrm{Net}_i^{\mathrm{Out}}) \end{cases} \tag{14}$$

where $\mathrm{Net}_i^{\mathrm{In}}$ is the label of the misalignment parameters, and $\mathrm{Net}_i^{\mathrm{Out}}$ is the output data of the training data set. Because accuracy rate is easier than loss function to interpret and monitor during the training phase, we define the accuracy rate as the evaluation of the final model accuracy:

$$\mathrm{Acc} = \frac{m}{n} \times 100\% \tag{15}$$

where m is the number of the predicted value, which satisfies the requirements of the coarse neural network and fine neural network. n is the sample size of the test data set.

3. Result

3.1. Configuration of the Simulation

In our simulations, the adopted neural network was trained on a laptop with an Intel i7 9750h processor, 16 GB RAM and

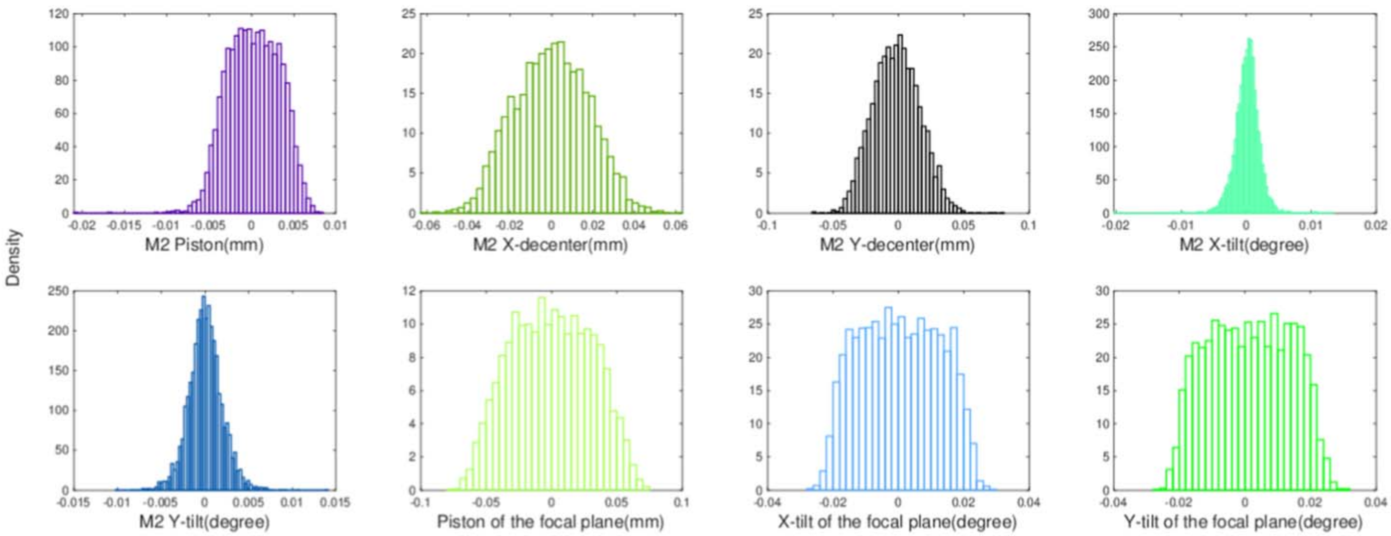

Figure 12. The error of the misalignment parameter distribution. The eight subfigures describe the error distributions of eight misalignment DOFs after two-step active alignment. The error distribution of each DOF is nearly a normal distribution after alignment, with over 90% position errors below 5 μm and over 90% angle positions below 5″. Furthermore, we added the units on the caption of each sub-image.

an Nvidia GTX 1660ti laptop graphics card with 6 GB of VRAM. TensorFlow, a widely used Python deep learning library, was utilized in neural network training. We randomly split the 10,000 stellar images and the corresponding misalignment parameters acquired from the DDE programming to 70%, 20% and 10% as training, validation and testing data, respectively. Note that the measurable parameters are fitted by the low-order Zernike polynomials to simplify the training model. The model can be trained successfully with a laptop and the prediction of the misalignment parameters of the two-step neural networks is almost real-time. The parameters (learning rate, loss function, active function) are updated in the networks for 400 epochs by using Optuna, which is an automatic hyperparameter optimization software framework, and it features an imperative, define-by-run style user API (Akiba et al. 2019). By using dropout to prevent the neural networks from overfitting, loss function can converge after training 400 epochs as displayed in Figure 7.

3.2. Simulation Results

In the simulation of the training data set, the range of the position is (–1 mm, 1 mm) and the range of the tilt-tip angle is (–5′, 5′). The stellar images are generated by ray tracing with random misalignment parameters in the range, which are shown in the right column of Figure 8. The three measurable parameters of the PSF are displayed in the middle column of Figure 8, and then fitted to 10 low-order Zernike polynomials as depicted in the left of Figure 8. The fitted low-order Zernike polynomials as the input and the corresponding label are the misalignment parameters. During training, the loss function converged quickly, as shown in Figure 7. After two-step active alignment by using a coarse neural network and fine neural network, the telescope can be calibrated precisely. The stellar images of the calibrated telescope are featured in Figure 9. The spot diagram is very small except for the four PSFs at the corners, which are out of the working field. This phenomenon is more obvious in Figure 10; for the 1000 test data set, the root mean square (rms) of the spot diagram of 1000 testing data sets at five FOVs is distributed randomly in the range of 50–200 μm. After two-step active alignment, the rms of the test samples in Figure 11 is mainly below 18 μm. The error of the misalignment parameter distribution is displayed in Figure 12. The first five pictures are the misalignment parameters of the second mirror, and the last three pictures are the misalignment parameters for the focal plane. The errors are distributed like a Gaussian function, and the position errors of misalignment parameters are less than 5 μm for decenter and less than 5″ for tip-tilt in more than 90% of the cases. The results confirm that the metrology proposed in this work is very accurate to actively align the telescope.

4. Conclusion

A novel two-step active alignment metrology based on coarse and fine neural networks is proposed in this work. The model calculates the misalignments based on stellar images of wide-field telescopes, and the two-step neural network can output the misalignment parameters of the optical system directly once it is well trained. Compared to the conventional field-dependent aberration approaches, this method is simpler in the system and higher in the calculating speed. Simulations are implemented to determine that the two-step neural network can be trained to calculate the misalignment parameters efficiently and accurately. Currently, the two-step neural network does not consider gravitational deformation of the primary mirror. Such powerful learning ability can also be used to continue predicting the deformation of the primary mirror for better applicability. Future work is considered to generate the training data set through the experimental system, which can be used to actively align the misalignments of Mephisto. This work represents a feasible and easily-implemented method to improve the efficiency and accuracy of active alignment metrology. Besides laboratory alignment, the metrology proposed in this study aims to maintain image quality during observation, with relatively low misalignment values mostly resulting from gravitational deformation. This method also has broad application prospects in an off-axis system and the optical system which contains a freeform surface.

Acknowledgments

This work was supported by the National Natural Science Foundation of China (Grant Nos. U1931207 and 12173062) and the project of Multi-channel Photometric Survey Telescope. The authors acknowledge Dr. Zhou Chen at the Institute of Space Science and Technology for helpful discussions on artificial network designs.

References

Akiba, T., Sano, S., Yanase, T., Ohta, T., & Koyama, M. 2019, in Proc. 25th ACM SIGKDD Int. Conf. on Knowledge Discovery & Data Mining, 2623
Benitez, N., Dupke, R., Moles, M., et al. 2014, arXiv:1403.5237
Bloemhof, E. E., An, X., Kuan, G., et al. 2012, ApOpt, 51, 394
Bo, L. 2021, Research on alignment method of Astronomical Optical Telescope based on star image characteristics, Thesis, University of CAS
Chen, Z., Jin, M., Deng, Y., et al. 2019, JGRA, 124, 790
Chueca, S., Marín-Franch, A., Cenarro, A. J., et al. 2012, Proc. SPIE, 8450, 84500I
Claver, C. F., Chandrasekharan, S., Liang, M., et al. 2012, Proc. SPIE, 8444, 84444P
Copeland, E. J., Sami, M., & Tsujikawa, S. 2006, IJMPD, 15, 1753
Crawford, D. L. 1966, in International Astronomical Union Symp, 27, International Council of Scientific Unions, (London: Academic Press)
Kasliwal, M., Cannella, C., Bagdasaryan, A., et al. 2019, PASP, 131, 038003
Lee, H., Dalton, G. B., Tosh, I. A., & Kim, S.-W. 2007, OExpr, 15, 3127
Li, Z., Lu, H., & Yuan, X. 2015a, ChOpL, 13, 111101
Li, Z., Yuan, X., & Cui, X. 2015b, MNRAS, 449, 425
Li, Z., Yuan, X., Zhang, K., & Li, B. 2020, Proc. SPIE, 203, 112030A
Luppino, G., & Kaiser, N. 1997, ApJ, 475, 20
Manuel, A. M., Phillion, D. W., Olivier, S. S., Baker, K. L., & Cannon, B. 2010, OExpr, 18, 1528
Sebag, J., Gressler, W., Liang, M., et al. 2016, Proc. SPIE, 9906, 99063E
Shack, R. V., & Thompson, K. 1980, Proc. SPIE, 251, 146
Su, D. 1989, AcASn, 30, 106
Tang, R., Zeng, F., Chen, Z., et al. 2020, Atmos, 11, 316
Thompson, K. P., Schmid, T., & Rolland, J. P. 2008, OExpr, 16, 20345
Wetherell, W., & Rimmer, M. 1972, ApOpt, 11, 2817
Xin, B., Claver, C., Liang, M., et al. 2015, ApOpt, 54, 9045
Yu, Q. 2020, The Innovation, 1, 100063
Yuan, X., Li, Z., Liu, X., et al. 2020, Proc. SPIE, 11445, 114457M
Zhang, K. 2016, Optical design based on Delano diagram method and research on Antarctic near-infrared skyscraper telescope, Dissertation, University of CAS